Supporting Information

A Tripodia Wheeled Mobile Robot Driven by Liquid Metal Motor

Rui Xue[a], Wenshang Guo[a], Ye Tao[a, b], Yukun Ren[a*]

[a]State Key Laboratory of Robotics and System, Harbin Institute of Technology, West Da-zhi Street 92, Harbin, Heilongjiang 150001, People's Republic of China. Email: rykhit@hit.edu.cn

[b]School of Engineering and Applied Sciences and Department of Physics Harvard University, 9 Oxford Street, Cambridge, MA 02138, USA. Email: ytao@seas.harvard.edu

Keywords: liquid metal, EGaIn, interfacial tension, soft motor, wheeled mobile robots

This material gives supporting information in the paper:

SI Appendix 1. Design and fabrication information of the mobile chassis.

SI Appendix 2. Boost time of the DC Power supply

SI Appendix 3. Redox reaction on LMDs at a high current density.

SI Appendix 4. Force analysis of the driven wheel in the steady operation state.

SI Appendix 5. Image recognition processing eccentricity distance of the LMD

SI Appendix 6. Experiment of mobile robot performance.

SI Appendix 7. Control module of the tripodia wheeled mobile robot.

Supplementary movie:

Movie S1. The demonstration of mobile chassis moving functions.

Movie S2. Morphologic changes of liquid metal during robot startup.

Movie S3. The surface of LMD at high current density.

Movie S4. The electrically induced flow of fluid along the surface of LMD

Movie S5. Motion function demonstration of 3-WMR.

SI Appendix 1. Design and fabrication information of the mobile chassis

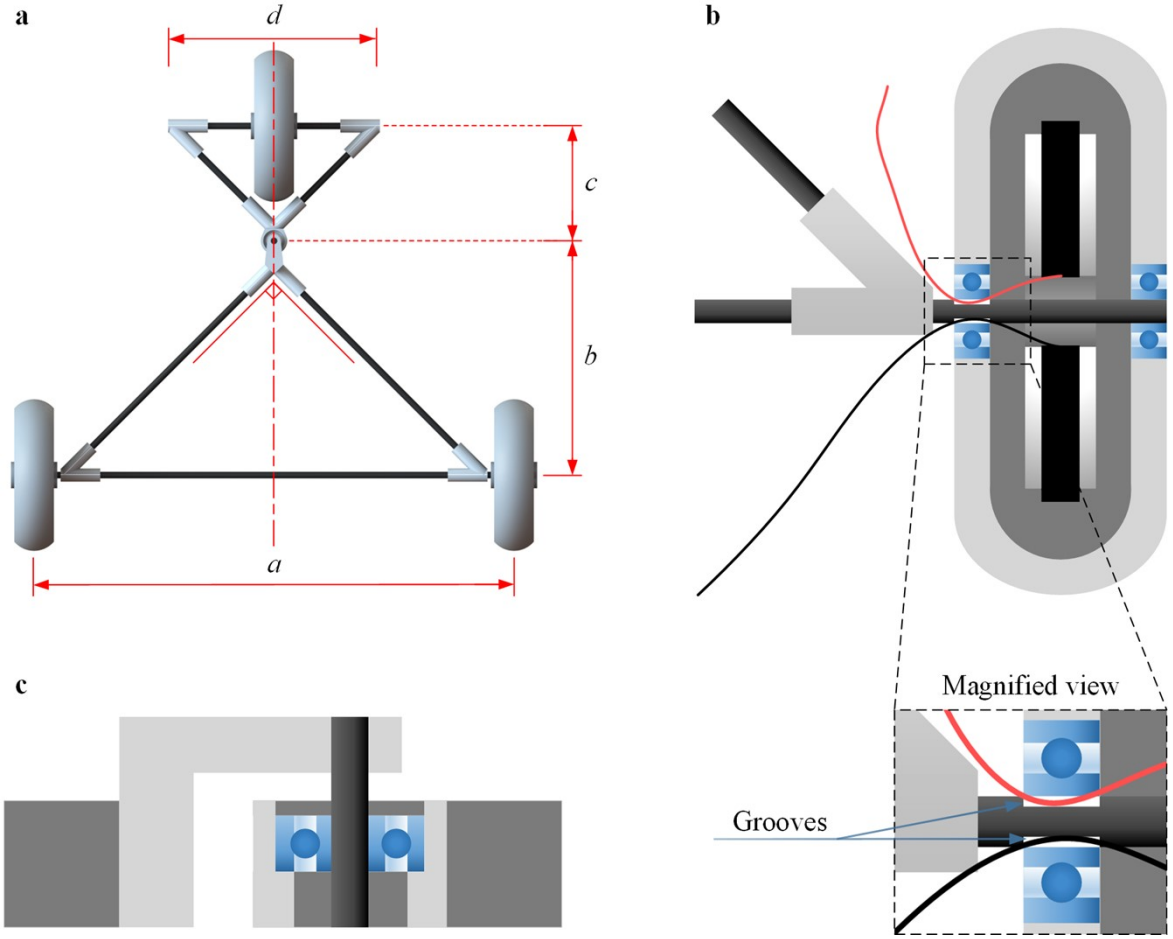

Figure S1. Detailed sizes and description of each part. (a) Top-view of the mobile chassis with related design sizes. (b) Top section view of the driven wheel. (c) Side section view of the steering device.

The isosceles right triangles frame of the driven and auxiliary parts is made of carbon fiber rods and a 3D printing connector. As shown in Figure S1 (a), the former owns a base of a=175 mm and a height of b=83 mm and the latter owns a base of c=40 mm and a height of d=68 mm.

Each driven wheel contains an electrode holder (with a pair of graphite electrodes) and a pair of ceramic bearings, they share the same axle through fixing the holder and the inner ring of ceramic bearing, while the driven wheel is relatively fixed with the outer ring of the ceramic bearing. Two enameled wires (connect the positive and negative poles of the power supply separately) are respectively attached to the graphite electrodes through the grooves of the shaft in the position where the driven wheel and the ceramic bearing contact to conduct the current (Figure S1 (b)). Another thing worth mentioning is that the outer wheel contour line of the cross-section of the driven/passive wheels is a curve. this design is to make sure the

wheels contacting with the ground is point contact in order to reduce the influence of assembly error in the working state.

The steering device works through a bearing: the inner ring of the bearing, the steering shaft, the 3D-printed V-shaped front steering frame, and the driving part are relatively fixed one by one through UV glue. The same installation method is applied to the latter part: including the outer ring of the bearing, the 3D-printed V-shaped rear steering frame, and the driving part (Figure S1 (c)).

The detailed design parameters of the structural accessories used by the mobile chassis are shown in Table S1.

Table S1. Properties of parts of the 3-wheeled mobile robot.

Part	Weight (Density)
Circuit Board (m_C)	66.44 g
Battery (m_B)	71.59 g
Robot (m_R)	19.35 g
LMD (m_{LMD})	5.58 g/cm^3
Working electrolyte ($m_{electrolyte}$)	1~2 g (according to the w_{LMD} in each driven wheel)

SI Appendix 2. Boost time of the DC Power supply

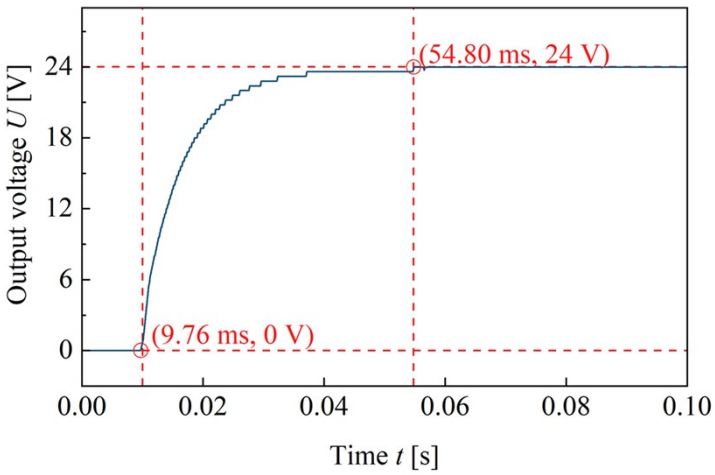

Figure S2. Test results of boost time of DC power supply.

Utilizing an oscilloscope (DPO2014b, Tektronix, USA) to measure the boost time of the DC power supply in the experiment. During the test result shown in Figure S2, it takes approximately 45 ms to rise from 0 to 24 V.

SI Appendix 3. Redox reaction on LMDs at a high current density

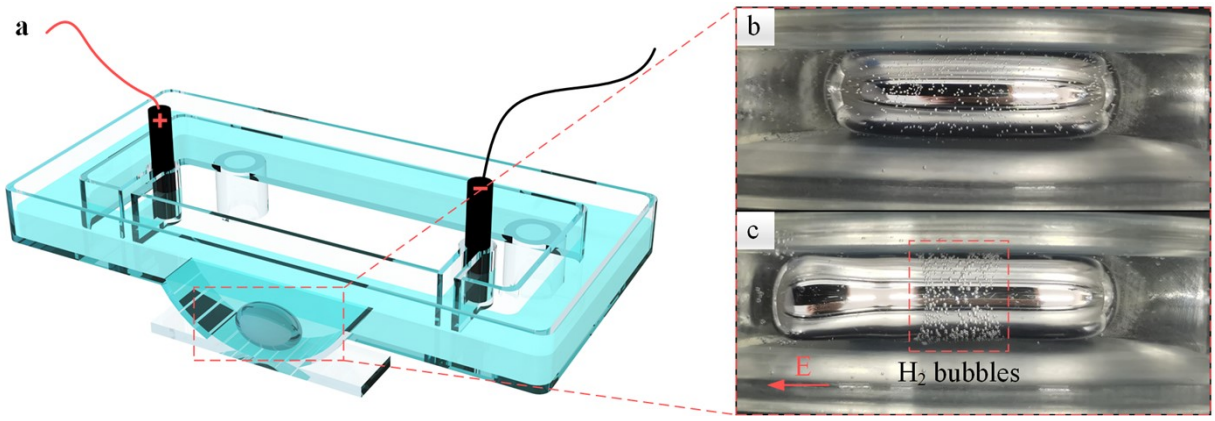

Figure S3. Redox reaction on LMDs. (a) Experimental channel to observe the redox reaction phenomenon. (b) Magnified top-view of LMD without applying an electric field. (c) Magnified top-view of LMD under an electro induced redox reaction.

To observe the LMD in the redox reaction phenomenon caused by the high background electric field, a rectangular circle channel was designed by 3D printing as shown in Figure S3 (a). A half-wheel chamber referring to the prototype of the driven wheel from the mobile chassis is located in the long edge of the channel for holding the LMD. the position of double electrodes is away from the chamber to avoid the influence of the bubbles generated by the electrolysis reaction in observation.

As shown in Figure S3 (b), in the absence of an applied electric field, the LMD rest at the bottom of the chamber, and its surface is covered with bubbles uniformly according to Equation (S1).

$$2Ga+2NaOH+2H_2O=2NaGaO+3H_2\uparrow \quad (S1)$$

After applying a dense electric field, both ends of the LMD stretch outwards respectively under the combined action of CEW and redox. All H_2 bubbles gather in the central position as shown in Figure S3 (c). Taking this gathering region as a boundary, the shape of LMD in the near anode side is more regular than the other opposite side which shows a low interfacial tension suffering here.

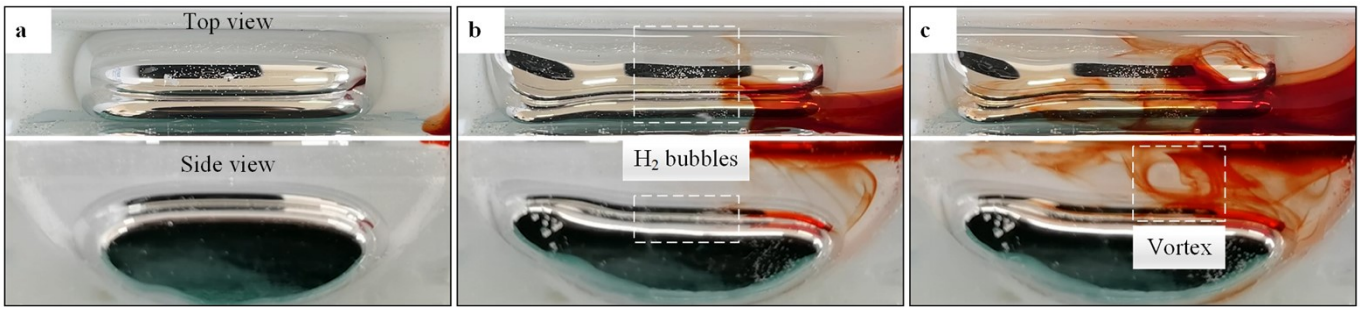

Figure S4. Electric flow on LM droplet surface. (a) top-view and side-view of LMD without applying an electric field.

(b) Bubbles congregated at the boundary between the oxidized region and non-oxidized region. (c) a vortex generated from the interfacial tension gradient.

As shown in Fig. S3 (a), the red ink is chosen to trace the fluid flow. After applying an electric field shown in Fig. S3 (b), the bubbles rapidly gathered in the middle of the LMD which was the boundary between the oxidized region and non-oxidized region. The fluid with ink began to flow along the surface of LMD from its near positive side. When the fluid reached the middle boundary, it started to flow upward instead of along its original direction and a vortex was generated here as shown in Fig. S3 (c).

SI Appendix 4. Force analysis of the driven wheel in the steady operation state

7 different forces are acting on the driven wheel as shown in Figure 2 h when the mobile chassis working steadily: the viscous resistance $\mathbf{F}_{\mathrm{LMD}}$ and eccentric torque $\mathbf{M}_{\mathrm{LMD}}$ from the LMD, the rolling friction $\mathbf{F}_{\mathrm{r}}$ from the ground, a viscous resistance $\mathbf{F}_{\mathrm{S}}$ from the solution inside the driven wheel, a pair of the same bearing friction torques $\mathbf{M}_1$ and $\mathbf{M}_2$, and the gravity force **G**. Among them, the $\mathbf{F}_{\mathrm{LMD}}$ and $\mathbf{M}_{\mathrm{LMD}}$ (marked with red) from the LMD are the impetus to drive the wheel. The $\mathbf{F}_{\mathrm{r}}$, $\mathbf{F}_{\mathrm{S}}$, $\mathbf{M}_1$, $\mathbf{M}_2$, (marked with blue) are the obstruction to the rotating motion. When the driven wheel operates in the steady-state, the effect of these 6 forces (except the gravity **G**) is balanced from physical constraint as follows:

$$\mathbf{F}_{\mathrm{LMD}}(R\text{-}t)+\mathbf{M}_{\mathrm{LMD}}=\mathbf{F}_{\mathrm{r}}R+\mathbf{F}_{\mathrm{S}}(R\text{-}t)+\mathbf{M}_1+\mathbf{M}_2 \tag{3}$$

$$\mathbf{M}_{\mathrm{LMD}}=l\mathbf{g}m_{\mathrm{LMD}} \tag{4}$$

$$\mathbf{F}_{\mathrm{r}}=\mu(m_{\mathrm{LMD}}+m_{\mathrm{C}}+m_{\mathrm{L}})\mathbf{g} \tag{5}$$

$$\mathbf{F}_{\mathrm{S}}=\eta_{\mathrm{S}}S\left(\frac{\mathrm{d}\boldsymbol{\omega}(R\text{-}t)}{\mathrm{d}y}\right) \tag{6}$$

where R (22.5 mm)denotes the radius of the driven wheel, t (1 mm) denotes the thickness of the driven wheel wall, $m_{\mathrm{LMD/C/L}}$ denotes the mass of the LMD/chassis/load, g denotes gravitational acceleration, l denotes the horizontal distance between the barycenter of LMD and wheel center, μ denotes the coefficient of rolling friction between driven wheels and the ground, η_{S} denotes the dynamic viscosity of the solution, S denotes the action area of $\mathbf{F}_{\mathrm{S}}$, $\boldsymbol{\omega}$ denotes the steady rotating speed of the driven wheel, y denotes the equivalent depth of the alkaline solution.

Among them, R, t, $m_{\mathrm{LMD/C/L}}$, g, μ, η_{S} are constants. The S and y are almost unchanged through observing the steady alkaline solution. At the same time, according to the image recognition analysis results, the l varies very little within the range of operating voltage. Besides this, The radius of the wheel is much greater than its wall thickness. Hence, we treated all of them as constants for simplification. Then the relationship between the speed of driven wheel **u** and its several influence factors below:

$$\mathbf{u}=\boldsymbol{\omega}R=K_1\left(\mathbf{F}_{\mathrm{LMD}}+\left(\frac{lg}{R}-K_3\right)m_{\mathrm{LMD}}-K_3m_{\mathrm{L}}-K_2\right) \tag{S6}$$

$$K_1 = \frac{y}{\eta_S S} \tag{S7}$$

$$K_2 = \frac{\mathbf{M}_1 + \mathbf{M}_2}{R} + \mu g m_C \tag{S8}$$

$$K_3 = \mu g \tag{S9}$$

SI Appendix 5. Image recognition processing eccentricity distance of the LMD

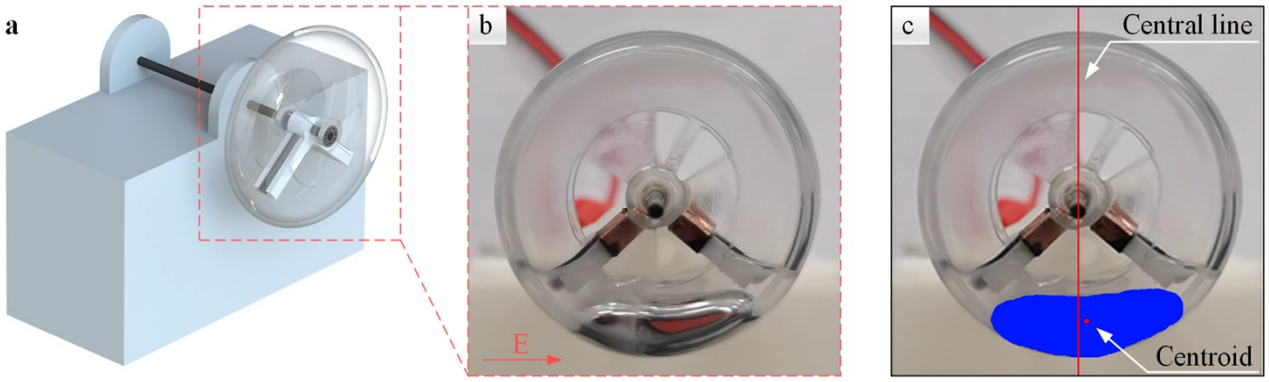

Figure S5. Estimation experiment for eccentricity distance of the LMD. (a) A simple test platform for the single driven wheel. (b) The real situation of droplet deformation. (c) Image recognition result of droplet deformation.

The single driven wheel was suspended in midair from a structure as shown in Figure S5 (a), When the driven wheel starts to rotate stably, the LMD moves along the electric field line in the wheel bottom as shown in Figure S5 (b).

A program was developed to identify the whole droplet area when applying an electric field: The vertical line passing through the center of the rotating axis was firstly taken as the central line. Then the droplet area was marked blue and its centroid was marked as well. Finally, the horizontal distance from the central line and centroid was calculated as the eccentricity distance of the LMD shown in Figure S5 (c).

SI Appendix 6. Experiment of mobile chassis performance

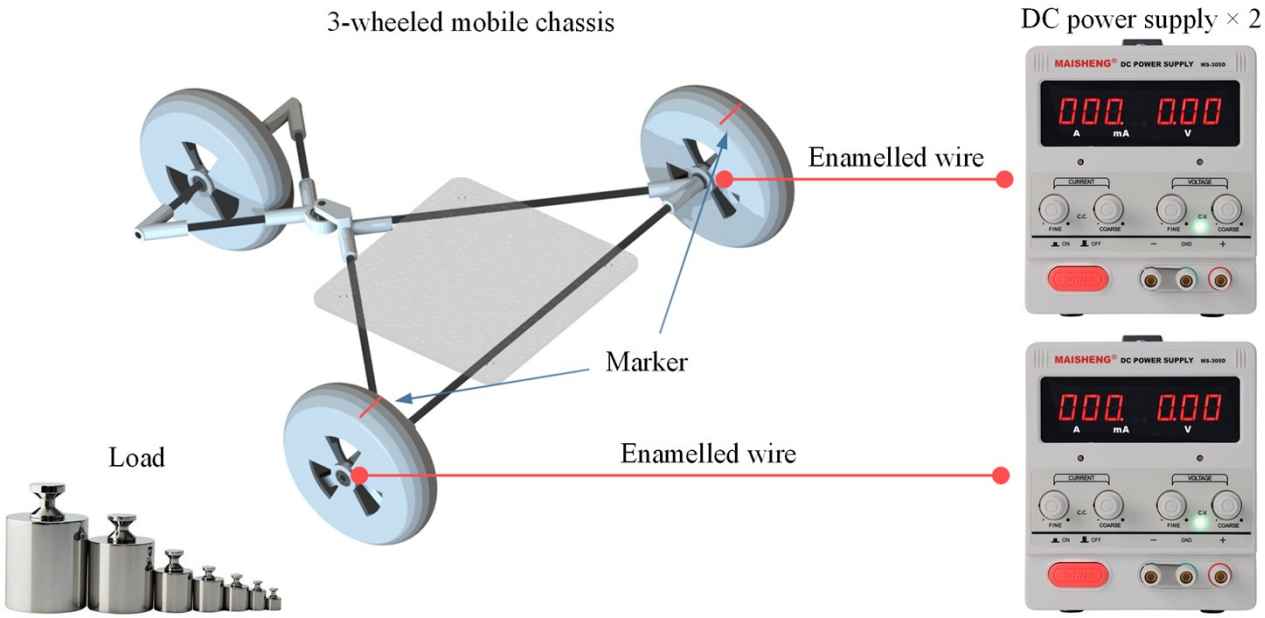

Figure S6. Experimental circumstance for the performance test of 3-wheeled mobile chassis.

As shown in Figure S6, two independent power supplies are settled to power double driven wheels through enamelled wires respectively. A series of standard loads are utilized for providing a load of 40/80/120/160 g in Figure 3 (d). All experimental moving speeds of mobile chassis in different performance tests are calculated through the markers on the driven wheels.

SI Appendix 7. Control module of the tripodia wheeled mobile robot

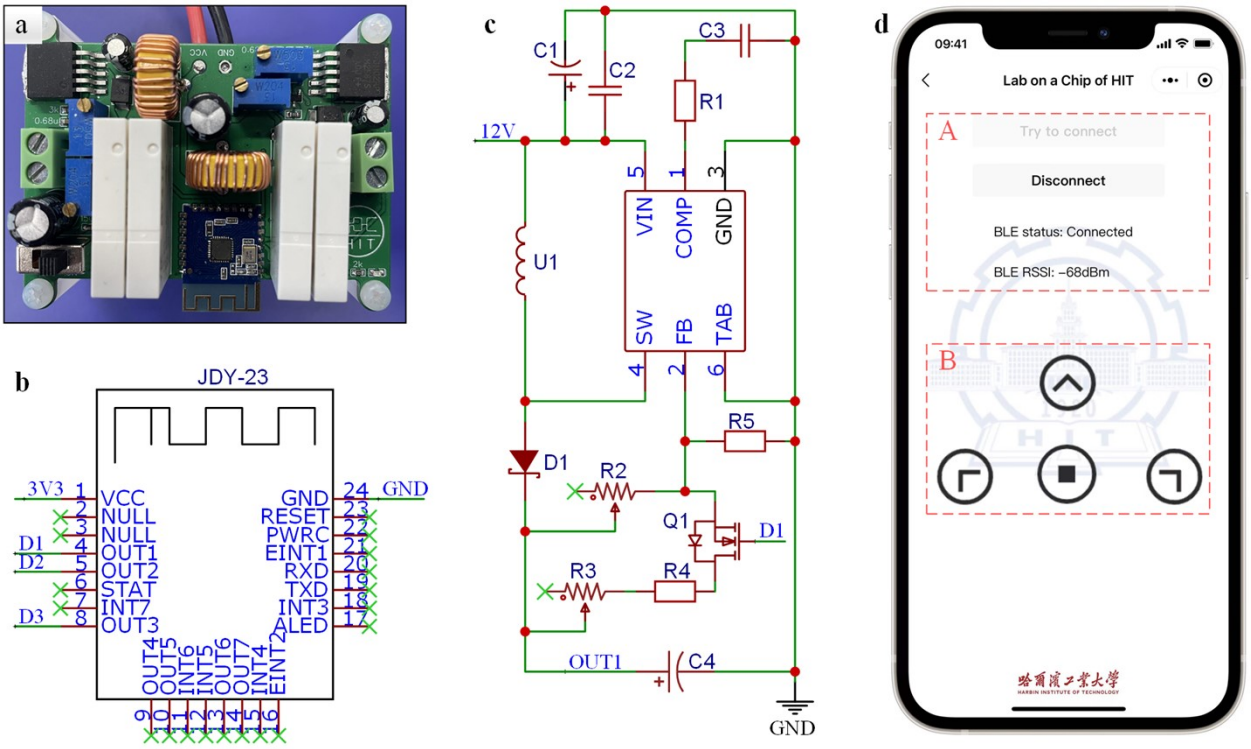

Figure S7. Control circuit and APP of mobile robot. (a) Photo of the control board. (b) Schematic diagram of Bluetooth Low Energy (BLE) module. (c) Circuit diagram of booster module. (d) Control application operation interface.

Figure S7 (a) shows the physical view of the tripodia wheeled mobile robot control circuit which consists of a boost module, voltage switching module, and BLE module. Among them, The BLE module (Figure S7 (b)) owns the IO control function, which provides conditions for the remote control of triode and MOS tube status for mobile phones. The boost module (Figure S7 (c)) is composed of the boost chip, the NPN MOS tube, and the surrounding circuit. Its main function is to increase the output voltage of lithium battery from 12 V to 15 V or 20 V for driving vehicle operation. MOS tube Q1 is used to control the feedback circuit of the boost chip by two different outputs.

A control application has been developed and its operation interface is displayed in Figure S7 (d). The two buttons in area A are used to manually switch the connection disconnection status of the Bluetooth connection and display the current Bluetooth connection status and signal strength. The four buttons in area B are used to control the robot to move forward, turn left, turn right and break. The corresponding control APP is developed on the smartphone and written in JavaScript.

The detailed parameter of voltage, current, and power consumption of the tripodia wheeled mobile robot are shown in Table S2,S3, and S4.

Table S2. The measuring output voltage of the battery and the applied volatge of driven wheels in 3 different working conditions.

Function	Battery [V]	Left wheel [V]	Right wheel [V]
Forward	12.5	19.8	19.9
Left steering	12.5	15.2	19.9
Right steering	12.5	19.8	15

Table S3. The measuring output current of the battery and applied currents of driven wheels in 3 different working conditions.

Function	Battery [A]	Left wheelt [A]	Right wheel [A]
Forward	0.90	0.19	0.20
Left steering	0.58	0.14	0.20
Right steering	0.61	0.20	0.15

Table S4. The calculated power consumption of the battery and driven wheels.

Function	Battery [W]	Left wheel [W]	Right wheel [W]	Output [W]
Forward	11.2	3.93	3.98	7.91
Left steering	7.3	2.13	4.04	6.17
Right steering	7.7	4.00	2.19	6.19